JOURNAL OF Applied Polymer SCIENCE

Effect of nano-titanium nitride on thermal insulating and flame-retardant performances of phenolic foam

Qiulong Li,[1,2] Lin Chen,[1,2] Xiaohai Li,[1,2] Jinjin Zhang,[1,2] Kang Zheng,[1,2] Xian Zhang,[1,2] Xingyou Tian[1,2]

[1]Institute of Applied Technology, Hefei Institutes of Physical Science, Chinese Academy of Sciences, Hefei 230031, People's Republic of China

[2]Key Laboratory of Materials Physics, Institute of Solid State Physics, Chinese Academy of Sciences, Hefei 230031, People's Republic of China

Correspondence to: X. Y. Tian (E-mail: xytian@issp.ac.cn)

ABSTRACT: In this work, titanium nitride (TiN) nanoparticles were employed to achieve enhanced thermal insulation and flame retardance of phenolic foam (PF)/TiN nanocomposites (PFTNs) via *in situ* polymerization. The morphologies of PFTNs were observed by scanning electron microscope and the images showed that the PFTNs have more uniform cell morphologies compared with pure PF. Thermal insulating properties of PFTNs were evaluated by thermal conductivity tests. The introduction of TiN obviously decreased the thermal conductivities of PF over a wide temperature range (−20 to 60 °C). Significantly, the thermal conductivity of PFTNs gradually decreased as the temperature increased from 30 to 60 °C, showing a contrary tendency with that of pure PF. Moreover, the thermal stability and flame-retardant properties of PFTNs were estimated by thermogravimetric analysis (TGA), UL-94 vertical burning and limited oxygen index (LOI) tests, respectively. The TGA and LOI results indicated that PFTNs possess enhanced thermal stabilities and fire-retardant performances with respect to the virgin PF. © 2016 Wiley Periodicals, Inc. J. Appl. Polym. Sci. **2016**, *133*, 43765.

KEYWORDS: composites; flame retardance; foams; thermal properties; thermogravimetric analysis (TGA)

Received 10 December 2015; accepted 7 April 2016
DOI: 10.1002/app.43765

INTRODUCTION

Polymer foams as thermal insulation materials are widely used in many fields, particularly in the building field, due to their good thermal insulation and mechanical properties, and light weight.[1,2] However, commercially used polymer foams such as polystyrene (PS),[3–5] polyurethane (PU),[6,7] polyvinyl chloride (PVC),[8] and polyethylene (PE)[9] foams, are easily combustible. They generate a large number of pungent smoke and toxic gases in the fire, which can seriously diminish the survival of human beings.[10–13] Lately, phenolic foam (PF) has been spotlighted owing to its advantageous features, such as excellent fire resistance, no dripping and low toxic gas release in fires as well as low cost, easy process, and a highly recycling capacity.[10,13–23] Furthermore, it also has a high thermal stability over a wide temperature range, keeping stable performance from −196 to 200 °C and high self-ignition temperature of 480 °C.[17,21,24–27] However, PF has low thermal insulating performance compared with other polymer foams due to its high thermal conductivity (0.4 W/mK) in the solid state, which severely restricts their application in many fields.[24] Hence, it is very important to improve its thermal insulating property.

For polymer porous materials, the improvement of their heat-insulating performance have been mainly achieved by refining the pore structures.[16,24,28–33] Moreover, it also can decrease their thermal conductivity by controlling their foam density.[34] For example, the study by Lei *et al.* indicated that the thermal conductivity of PF with mean pore size of 800 nm and foam density of 120 kg/m^3 can achieve 0.028 W/mK at 293 K.[28] Song *et al.* reported that the thermal conductivity of modified PF with 1.0 wt % multiwalled carbon nanotubes with 65.3 kg/m^3 is 0.058 W/mK at room temperature.[24] Carvalho *et al.* investigated the thermal conductivity of PF with density of 120 kg/m^3 and compared them to lignin-PF with density of 450 kg/m^3. They reported that their thermal conductivities are 0.057 and 0.072 W/mK at room temperature, respectively.[35]

Unfortunately, most of researches focused on investigating the thermal conductivity of PF at only one temperature point.[24,29] As we know, PFs are applied in diverse applications, such as civil construction,[36] passenger and military aircrafts, marines and electronic fields[28] at complex temperature conditions. Therefore, it is extremely important to study the thermal conductivities of PFs over a wide range of temperature, which are

evidently significant to the practical applications of PF. To the best of our knowledge, there are no reports related to the study of the thermal conductivity of PF over a wide range of temperatures.

This study focused on improving the thermal insulating and flame-retardant properties of PF by introducing TiN nanoparticles via *in situ* polymerization. It is well known that the *in situ* polymerization can effectively prevent the agglomeration of nanoparticles in the polymer matrix.[37] The thermal insulating properties of PFTNs were investigated by thermal conductivity tests (TCT) over a wide range of temperatures, which is highly significant in their applications. The cell morphologies were evaluated by scanning electron microscope (SEM). Moreover, the thermal stability at elevated temperatures was evaluated by measuring the weight loss using thermogravimetric analysis (TGA). Flame retardant property was characterized by vertical flame tests (VFT) and limiting oxygen index (LOI) tests.

EXPERIMENTAL

Materials

Phenol and aqueous formaldehyde solution (37 wt %) were both purchased from Sinopharm Chemical Reagent Co., Ltd. (Shanghai, China). Sodium hydroxide and hydrochloric acid were both provided by Shanghai SuYi Chemical Co., Ltd (Shanghai, China). Polysorbate-80 (surfactant), n-pentane (foaming agent) and *p*-toluenesulfonic acid (curing agent) were all offered by Tianjin Guangfu fine Chemical Research Institute (Tianjin, China). Titanium nitride nanoparticles (TiN nanoparticles, radiant barrier agent) (30 nm) was purchased by Hefei Kaier nanoscience and technology Co., Ltd. (Hefei, China). All reagents were analytically pure agent and used without further purification.

Synthesis of Thermoset Phenolic Resin (PR) and PR/TiN Nanocomposites (PRTNs) via *In Situ*-Polymerization

First, different concentrations of TiN nanoparticles (0.5, 1, 2, 3, and 4 wt % with respect to PF) were added to the formaldehyde solution (150 g, 1.85 mol) and dispersed ultrasonically followed by stirring with a magnetic stirrer for 30 min, forming a supernatant solution denoted as TNFs. A 500 mL three-neck round-bottom glass flask fitted with a separating funnel, a reflux condenser, and a mechanical stirrer was fastened to a thermostat water bath. Phenol (94 g, 1 mol) and sodium hydroxide solution (50 g, 0.25 mol, 20 wt %) were added into the flask. The mixture was stirred and the water bath was heated to 85 °C. Then, TNFs was dropwise added to the flask which was kept at 85 °C for 3.5 h with constant agitation. Then, the polymerization products were poured into a 500 mL glass beaker fitted with a mechanical stirrer until cooling it to room temperature. Next, hydrochloric acid (36 wt %, 0.25 mol, and 25.3 g) was dropwise added to the beaker for neutralizing with constant agitation at 600 rpm. Followed by delaminating and reducing pressure distillation, the PRTNs were obtained, which were used for foaming. In order to acquire a comparison experiment, the pure PR was also synthesized under the same conditions with respect to the PRTNs.

Preparation of Pure PF and PFTNs

First, PRTNs (50 g), n-pentane (blowing agent, 4.5 g), and polysorbate-80 (2 g) were added into a 250 mL plastic beaker under rapid, 600 rpm, stirring and the stirring continued for 2 min. Secondly, p-toluenesulfonic acid (5 g) was added into the beaker under continuous rapidly stirring with the same speed for 10 min. Finally, the viscous mixtures (40 g) were poured into a mold [length (L) × width (W) × thickness (T) =120 × 120 × 45 mm^3] quickly, and then cured and foamed at 75 °C for 90 min. Pure PF was prepared under identical conditions in order to compare the results and denote any differences in the properties of the foams. The foam samples were denoted as PFTN0.5, PFTN1, PFTN2, PFTN3, and PFTN4 with respect to the weight fraction of TiN nanoparticles. Foam samples were cut to identical blocks which were used for the various tests. The volume density of the foam samples was controlled at 42 ± 2 kg/m^3. The dosages of all raw materials were shown in Table I. Based on the above experimental procedure, the flow diagram of synthesis of PRTNs and preparation of PFTNs were performed as shown in Figure 1.

Characterization and Measurements

The morphologies of samples were observed under a Sirion-200 (FEI, The United States) SEM with an accelerating voltage of 10 kV.

The phase composition and the crystalline structure of TiN nanoparticles and the PF samples were characterize by XRD analysis (X'Pert, PANalytical Netherlands) with the 2θ range from 10° to 90°.

The specimens were dried at 50 °C for 12 h to remove the internal moisture before measuring their thermal conductivity, mechanical property, thermal stability, limit oxygen index (LOI), and mass. The thermal conductivity values of samples were measured by a HFM 436 Lambda-Heat flow meter (Netzsch, Germany) with the sample size of 120 × 120 × 45 mm^3 and the temperature range was from −20 to 60 °C, and all values reported in this article represent an average of the results for three tests. The experimental error was ±1 °C for temperature and ±0.5 mW/mK for thermal conductivity.

The compressive and tensile tests were carried out using an Instron universal material testing system (model 5567) at room temperature according to GB/T 8813-2008 and GB/T 9641-1988, respectively. The results showed in this study were an average of the data for four samples tests.

TGA was carried out by a Q5000 IR thermal gravimetric analyzer at a heating rate of 10 °C/min under nitrogen and air atmosphere, respectively. All the samples were kept at 5–10 mg in an open alumina pan and tested from room temperature to 700 °C. The experimental error was ±1 °C for temperature and ±0.1% for residual mass.

The underwriters' laboratories 94 (UL-94) vertically burning tests for specimens were performed on an AG5100A instrument (ZhuHai AnGui Instrument Company, China) and the dimensions of all samples were 100 × 10 × 5 mm^3.

The LOI values were measured using a JF-3 LOI test instrument (Jiangning Analytical Instrument, China), according to ASTM

Table I. Formulation for Pure PF and PFTNs with TiN Nanoparticles

Samples	Resin samples	Phenol (g)	Formaldehyde (g)	Sodium hydroxide (g)	TiN (g)
PF	PR	94	150	—	—
PFTN0.5	PRTN0.5	94	150	50	1.12
PFTN1	PRTN1	94	150	50	2.24
PFTN2	PRTN2	94	150	50	4.48
PFTN3	PRTN3	94	150	50	6.72
PFTN4	PRTN4	94	150	50	8.96

D2863-97 and the values shown in this article are an average of the results for four samples test.

Foam density, porosity, density of carbon-layer of foam after LOI tests, and cell density were calculated as follows: The length (L), width (W), and thickness (T) of the foam specimens tested for specimen density were 120, 120, and 45 mm, respectively. Actually, the density ρ (kg/m^3)[24] of foam samples are calculated as the ratio of foam mass M to geometrical volume V as shown in the following equation:

$$\rho_f = \frac{M}{V} = \frac{M}{L \times W \times T} \quad (1)$$

The values shown in this article are the average of four tests. Density of the solid phenolic specimens (ρ_s) was also measured to calculate the porosity of the phenolic foams. The void formation of the solid specimen was minimized during the curing process. The porosity of the foam samples with respect to the test variables was calculated using the following equation:

$$\text{Porosity} = \frac{\rho_s - \rho_f}{\rho_s} \times 100\% \quad (2)$$

where ρ_s and ρ_f are the previously measured solid and foam density, respectively. Furthermore, the foam porosity was measured using a Pore Master 60-GT automatic pore size analyzer (Quantachrome Instruments, The United States) at constant temperature 20 °C.

The density ρ′ (kg/m^3) of char skeleton of samples after LOI tests were calculated as the ratio of foam mass m to geometrical volume v as expressed in the following equation:

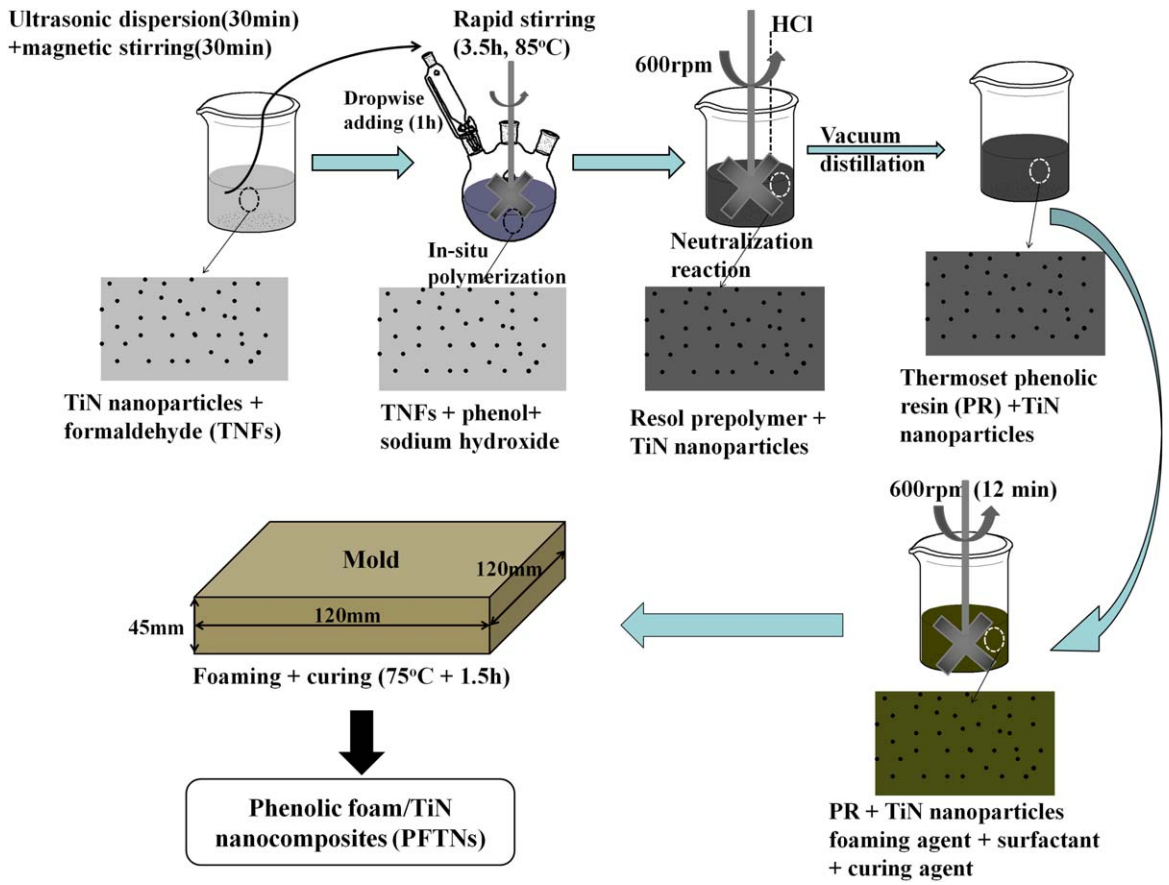

Figure 1. The flow diagram of synthesis of phenolic resin/TiN nanocomposites and preparation of phenolic foam/TiN nanocomposites. [Color figure can be viewed in the online issue, which is available at wileyonlinelibrary.com.]

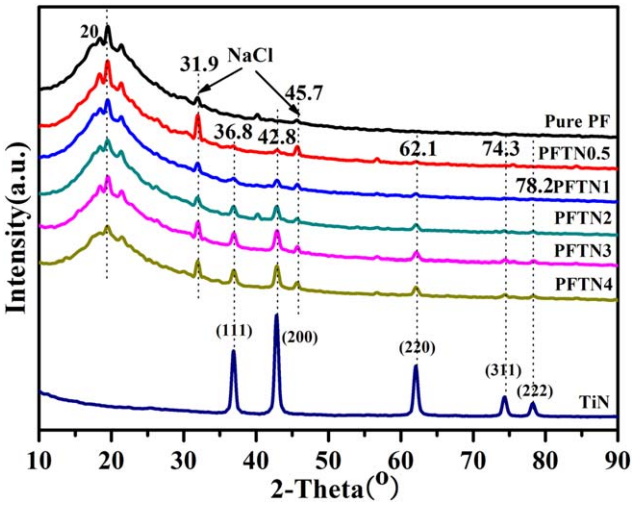

Figure 2. XRD patterns of pure PF, PFTNs, and TiN nanoparticles. [Color figure can be viewed in the online issue, which is available at wileyonlinelibrary.com.]

$$\rho' = \frac{m}{v} \tag{3}$$

The volume of samples after LOI tests was measured by water displacement method. The experimental error was ±0.0005 g for m and ±0.2 mL for v. The values shown in this article are an average of the results from four tests.

The cell density (N, cell/cm^3) which is number of cells per unit volume was calculated employing the following equation:

$$N = \frac{n}{V_f} = \frac{(V_{\text{total.cell}}/V_{\text{sphere}})}{V_f} = \frac{V_f - V_s}{V_{\text{sphere}} \times V_f} = \frac{L \times W \times T - V_s}{(4/3)\pi R^3 \times L \times W \times T} \tag{4}$$

The geometry of the cell was assumed to be a sphere (radius: $R = \bar{d}/2$) in order to calculate the cell density. And the calculated results by this assumption are approximate in this study. Where n is number of cells in a foam sample, V_f and V_s (50 cm^3) are the volume of foam sample and solid mixture of resin with foaming agent, surfactant and curing agent before foaming, respectively. $V_{\text{total cell}}$ and V_{sphere} are the volume of total cell and sphere, respectively. $\bar{d}$ is the mean cell size of foam samples, and the $\bar{d}$ was obtained by calculating the sizes of 200 cells in the SEM images through the Nano Measurer 1.2.

RESULTS AND DICUSSION

Foam Structures and Morphologies

The phase compositions of the pure PF and PFTNs were investigated by XRD analysis and their spectra are shown in Figure 2. The pure PF presents steamed bread peak around 20°, which is ascribed to the amorphous diffraction peak.[38–40] In addition, the characteristic diffraction peaks of sodium chloride (NaCl), which was obtained by neutralization reaction between hydrochloric acid and sodium hydroxide during the neutralization process of phenolic prepolymer, also appear at 31.9° and 45.7° in the XRD patterns.[41] It can be seen that the PFTNs show the same characteristic peaks of NaCl and amorphous diffraction peaks with respect to the pure PF. Remarkably, there are five peaks at 36.8°, 42.8°, 62.1°, 74.3°, and 78.2° appeared in the PFTNs' spectra, which are attributed to the characteristic diffraction peaks of TiN.[42,43] Moreover, the peaks' intensities increase with the increasing content of TiN nanoparticles, confirming that TiN nanoparticles have completely incorporated into the PR matrix. Additionally, by introducing the TiN nanoparticles, the color of the PFTNs appears as light black and it gradually turns darker as the content of the nanoparticles increased.

The microstructures of the pure PF and PFTNs were observed by SEM and the images are shown in Figure 3. The pure PF presents many circular and elliptical closed cells. The mean cell size of pure PF is 222.3 μm and cell sizes distribution is from 100 to 450 μm as shown in Figure 3(a). Markedly, the mean sizes and distributions of cells for the PFTNs become smaller and narrower in relation to the pure PF by the addition of TiN nanoparticles. For example, the PFTN1 displays the smallest mean cell size of 102.1 μm and narrow size distribution from 60 to 160 μm. This result may be explained that the introduction of TiN into the PF matrix forms a nucleating influence during foaming process and enhances the cells number per volume unit. Furthermore, the cells shape tends to be regular hexagon like a honeycomb.

As is known, a uniform cell shape and narrower cell sizes distribution may lead to an excellent thermal insulating property.[24] However, the average cell size and distribution gradually increases with further growth of TiN content. As the TiN increase to 4 wt %, the mean cell size increases to 162.0 μm and the cell sizes distribution also broaden (90–280 μm). Even so, these two parameters are evidently less than that of the pure PF. Cells are formed firstly on the TiN surface owing to the heterogeneous nucleation of nano-TiN. Meanwhile, the thermodynamics of the PF matrix is unstable and the cells will grow gradually.[44] Some neighboring cells will diffuse, contact together, and then collapse due to excessive heterogeneous nucleating point, resulting in formation of large cells. This result is mainly due to the interfacial tension. The viscosity of the phenolic/TiN composite resin has a sharp increase with the continuation of the curing process. The small and large cells are solidified gradually to form the cell sizes distribution, which can be confirmed by the SEM images. It is well known that smaller cell size may lead to higher cell density, which is an important parameter to evaluate the thermal insulating performance of PF foams.[24] The results above can also be explained as follows: The formation process of the PF has three stages: cell nucleation, cell growth, and cell stability. For the formation process of pure PF, cells can freely grow and the restriction of growth is very weak. Moreover, the cell wall thickness gradually becomes thinner in the last step. Therefore, a large number of cells will become very big, some cells will collapse, and the growth of other cells will be restricted because of expansion of the big cells. Hence, the pure PF presents inferior cell morphology, and it is verified by the SEM image. For the formation of the PFTNs, cells cannot freely grow and the growth will be restricted due to the existence of TiN nanoparticles in the matrix. With the growth of cells, the TiN nanoparticles will gradually embed into the cell walls, so the cell wall will reach

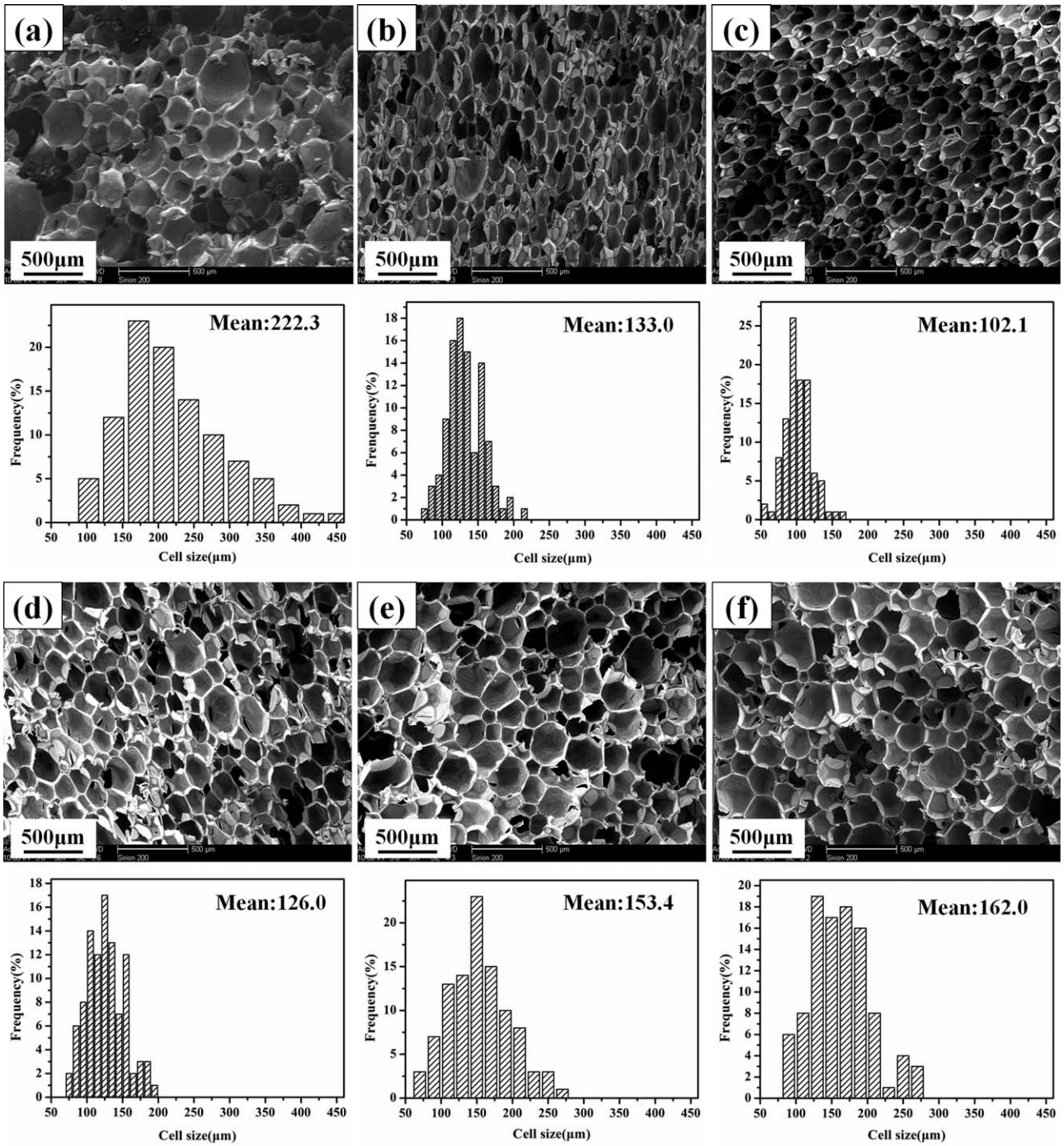

Figure 3. SEM images and the corresponding cell sizes distributions of (a) pure PF, (b) PFTN0.5, (c) PFTN1, (d) PFTN2, (e) PFTN3, and (f) PFTN4 (50×).

certain of thickness and will not become much thinner. For this reason, almost all cells can grow to a similar size.

To further analyze the foam morphology, the foam and cell densities and porosity were calculated and listed in Table II. Pure PF shows the lowest cell density of 1.6×10^5 cell/cm^3, which will lead to high thermal conductivity. Meanwhile, it also shows the lowest calculated porosity and tested porosity of 94.4 and 92.6%, respectively, which will result in poor mechanical property. The PFTNs have similar foam density to that of pure PF, attributing to the same mass of foam precursor. However, the PFTNs all show increased cell densities with respect to the pure PF. In addition, the porosities also increase by introducing TiN nanoparticles into PF. The higher cell density and porosity contribute to obtain a lower thermal conductivity and higher mechanical strength, respectively. Significantly, the PFTN1 presents a maximum cell density of 1.7×10^6 cell/cm^3 and the calculated and tested porosities are of 97.6 and 95.2%,

Table II. The Solid Density, Foam Density, Cell Density, Porosity, and Char Skeleton Density of Pure PF and PFTNs

Samples	Mean cell size (μm)	ρ_s (kg/m^3)	ρ_f (kg/m^3)	Calculated porosity (%)	Tested porosity (%)	Cell density N (cells/cm^3)	ρ' (kg/m^3)
PF	222.3 ± 9	773 ± 2	43 ± 2	94.4	92.6	1.6×10^5	103 ± 2
PFTN0.5	133.0 ± 5	1187 ± 2	43 ± 2	96.4	94.3	7.5×10^5	136 ± 2
PFTN1	102.1 ± 4	1644 ± 2	40 ± 2	97.6	95.2	1.7×10^6	148 ± 2
PFTN2	126.0 ± 4	1454 ± 2	42 ± 2	97.1	94.7	8.8×10^5	163 ± 2
PFTN3	153.4 ± 6	1377 ± 2	44 ± 2	96.8	93.5	4.9×10^5	161 ± 2
PFTN4	162.0 ± 7	1530 ± 2	42 ± 2	97.3	94.8	4.2×10^5	154 ± 2

respectively, indicating a lowest thermal conductivity and highest mechanical strength as compared with other PFTNs.

Thermal Conductivity

As we know, the thermal conductivity is an important parameter for evaluating the thermal insulating properties of polymer foam materials. For insulating foam materials, thermal transfer has four ways: heat transfer through the gas in the cells (λ_g) and the solid polymer (λ_s), heat radiation through the cells (λ_r), and heat convection through the gas in the cell (λ_c). Therefore, the total thermal conductivity (λ_t) of foam materials can be expressed as[35,45,46]:

$$\lambda_t = \lambda_g + \lambda_s + \lambda_r + \lambda_c \quad (5)$$

The thermal convection becomes significantly only when cell diameters are larger than 10 mm.[35] In consideration of the small cell diameters (<500 μm) for the pure PF and PFTNs, the parameter λ_c in the eq. (5) can be ignored. Therefore, the eq. (5) can be adjusted into:

$$\lambda_t = \lambda_g + \lambda_s + \lambda_r \quad (6)$$

In general, the λ_s is immediately related to the foam density. It is worth mentioning that all foam samples show similar λ_s due to similar foam density (see Table II) in the present work. It is noted that λ_g has inverse relationship with the porosity and cell density and λ_r is immediately related to the foam density and mean cell diameter.[33,47]

The thermal conductivity of the pure PF and PFTNs were measured from −20 to 60 °C and the curves versus temperature were shown in Figure 4. It was found that the thermal conductivity of the pure PF rises gradually from 34.3 mW/mK at −20 °C to 41.4 mW/mK at 60 °C with the increase of temperature, and less than 50 mW/mK, indicating that the PF can serve as a good thermal insulation material. The addition of TiN nanoparticles considerably decreases the thermal conductivity, as shown in Figure 4. Moreover, for the PFTN0.5, PFTN1 and PFTN2, as the increasing of temperature, the thermal conductivities rise from −20 to 30 °C and then decline from 30 to 60 °C. It is well known that, for conventional foam, the thermal conductivity gradually increases with the increasing temperature less than 80 °C, which will limits their applications at high temperatures.[46,48,49] However, by the introduction of TiN nanoparticles in conventional foams can effectively solve the problem of high thermal conductivity at high temperature. For the PFTN3 and PFTN4, the thermal conductivities also show similar variation tendency with increasing temperature, while the inflexions decrease to 20 °C.

To further investigate the influence of TiN nanoparticles on the thermal conductivity, the thermal conductivity curves with the

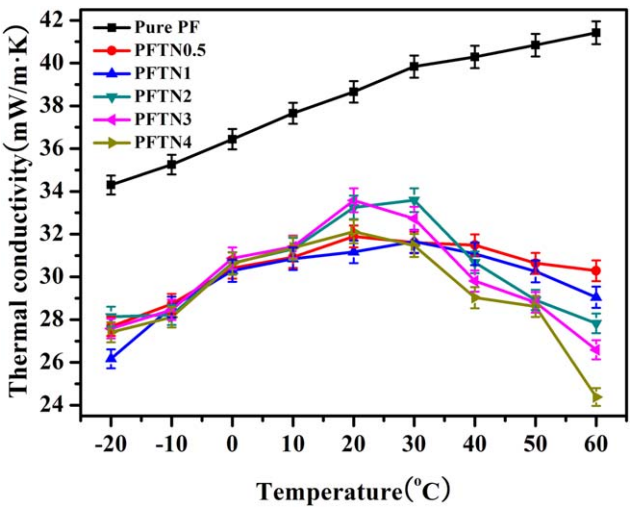

Figure 4. The relationship between thermal conductivities of pure PF and PFTNs and the temperatures. [Color figure can be viewed in the online issue, which is available at wileyonlinelibrary.com.]

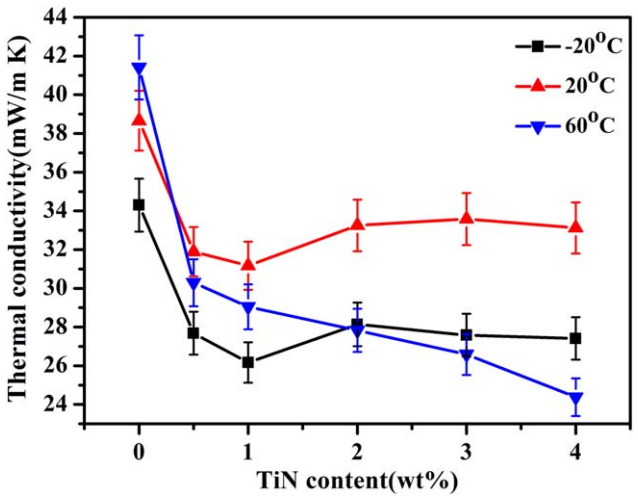

Figure 5. The thermal conductivities of PF and PFTNs at −20, 20, and 60 °C. [Color figure can be viewed in the online issue, which is available at wileyonlinelibrary.com.]

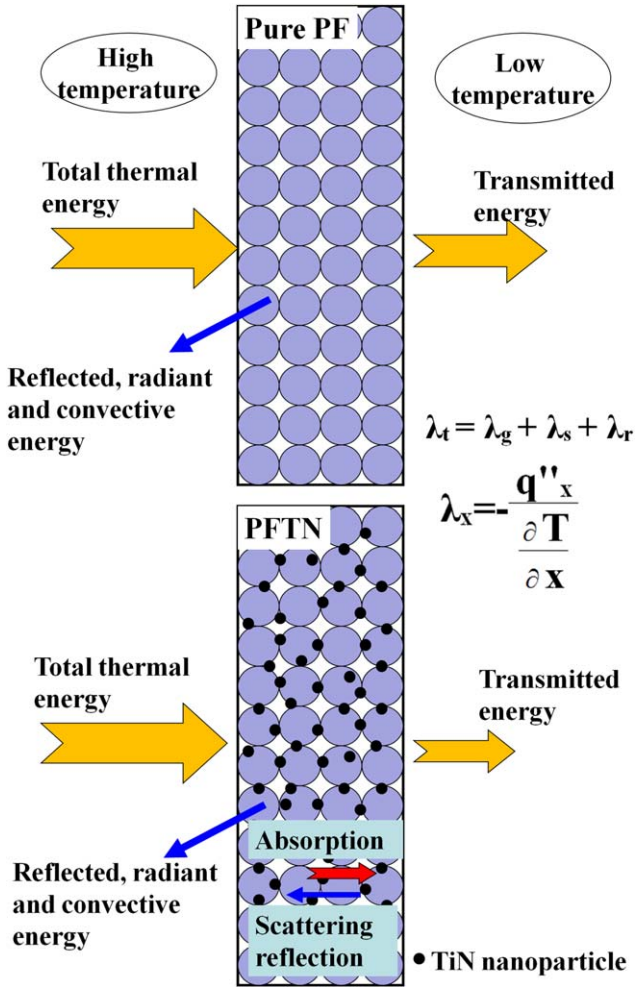

Figure 6. The model of thermal transfer for pure PF and modified PF with TiN nanoparticles. [Color figure can be viewed in the online issue, which is available at wileyonlinelibrary.com.]

amount of TiN at −20, 20 and 60 °C were shown in Figure 5. At low and room temperatures (−20 and 20 °C), the thermal conductivity dramatically reduce by the addition of nano-TiN. As the addition amount increases to 1 wt %, their values reach the minimum (26.2 and 31.2 mW/mK), which decrease by 23.7 and 19.4% with respect to the pure PF, in good agreement with the suggested results above. The lowest thermal conductivity can be attributed to the minimum ($\lambda_g + \lambda_r$), as a result of the maximum porosity and cell density and the minimum mean cell diameter.[31,50] However, the thermal conductivities increase as the further growth of TiN amount. Even so, their values are much less than that of the pure PF (see Figure 5). At high temperature, the thermal conductivity also markedly decreases after the introduction of TiN nanoparticles and it gradually declines with the increasing of nanoparticles. As the addition increases to 4 wt %, the thermal conductivity decreases to 24.4 mW/mK, drastically reduced by 41.1% as compared with that of the pure PF. For the pure PF, during the TCT, besides a small amount of heat are reflected, conducted and radiated back to the high temperature surface, a large amount of heat transfer to the low temperature surface by the conduction and radiation. For the low-density polymer foams (≦50 kg/m^3), heat radiation can easily transfer through foam matrix.[32]

During the foaming process of PFTNs, the TiN nanoparticles will gradually embed into the cell walls as discussed in previous section. Heat conduction and natural convection are important in measuring the conductivity for the present porous PFTNs foams. In PFTNs system, each TiN nanoparticle is encapsulated in phenolic resin with low thermal conductivity and these nanoparticles are separate in the phenolic matrix. They cannot form continuous networks for heat transfer. Hence, the nano-TiN cannot bring into play heat conduction during the TCT. Phonons are scattered in interfaces between TiN nanoparticle and phenolic resin, resulting in a decreased thermal conductivity.[51] In addition, the embedded TiN nanoparticles, which can act as an effective radiation blocking agent, significantly weaken the heat transfer during TCT. Therefore, it is different from the pure PF that some of the energy are scattered, reflected and absorbed by the embedded TiN nanoparticles back to the high temperature surface during TCT, as shown in Figure 6. According to Fourier's law, the formulation of thermal conductivity is defined as follows:

$$\lambda_x = -\frac{q''_x}{\frac{\partial T}{\partial x}} \quad (7)$$

Here, λ_x-thermal conductivity, x-the orientation of heat flux, q''_x-the density of heat flow in x orientation, $\frac{\partial T}{\partial x}$ is the gradient of temperature in x orientation. More addition of the TiN nanoparticles will lead to decreased q''_x. As a result, at high temperatures, the thermal conductivity decreases with the increase addition of TiN nanoparticles, which can explain above results in Figure 4.

Mechanical Property

Figure 7(a,b) show the curves of compressive strength and tensile strength as a function of nano-TiN content, respectively. From Figure 7, it can be clearly seen that the compressive and tensile strength increase with the increase of nano-TiN content, and then the compressive and tensile strength decrease while the nano-TiN content increases. The pure PF presents the lowest compressive strength (98.8 kPa) and tensile strength (131.4 kPa). When the dosage of nano-TiN is up to 1 wt %, the compressive strength and tensile strength reach the highest value. The PFTN1 shows the compressive and tensile strength of 110.5 and 145.7 kPa, which increased by 11.8 and 10.9%, respectively, compared with the pure PF. The reason was mainly due to the most uniform cell morphology, the lowest mean cell size, and the highest porosity and cell density of PFTN1 as shown in Figure 3 and Table II. The results of mechanical properties indicate that the introducing of a small amount of nano-TiN improves the mechanical strength of PF. However, when the dosage of nano-TiN is up to 4 wt %, the compressive and tensile strength of PFTN4 is 97.9 and 128.6 kPa, respectively, which was lower than that of the pure PF, indicating that the introduction of high nano-TiN content will reduce the mechanical properties of PF. From the compressive and tensile results, it can be seen that nano-TiN content shows a small effect on mechanical strength, and PF modified by 4 wt % nano-TiN displays the lowest compressive and tensile strength, compared with the pure PF.

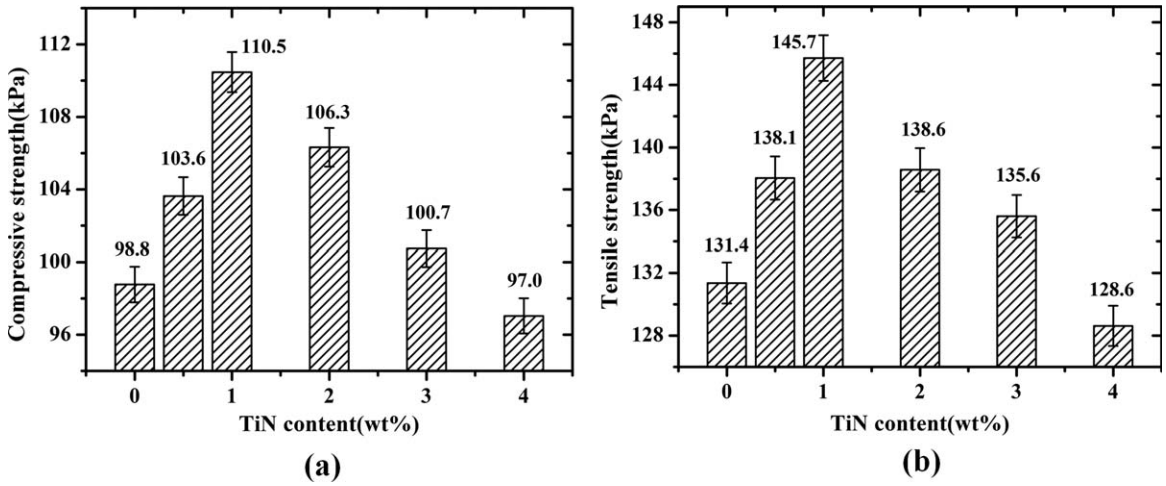

Figure 7. Mechanical strength of pure PF and PFTNs with different TiN content: (a) compressive strength and (b) tensile strength.

Thermal Stability

Figures 8 and 9 show the TGA and DTG curves of PFs with various content of nano-TiN in nitrogen and air atmosphere, respectively. Some relevant TGA and DTG data for pure PF and PFTN systems in nitrogen and air atmosphere are listed in Tables III and IV, respectively. The effect of nano-TiN content on thermal stability of PF in different atmosphere (nitrogen and air) is investigated as follows.

As shown in Figure 8, the pure PF degrades in two separate stages.[52,53] The PF only losses a fraction of weight in the first stage (250–350 °C). The lost weight was attributed to the release of the superfluous water, aldehyde, phenol, and short oligomers. In the second stage, from 350 to 700 °C, phenolic resin chains begin to fracture and further rapidly degrade into low molecular weight products.

After the introduction of TiN nanoparticles, the PFTNs also show two thermal degradation processes, similar with the degradation behavior of the pure PF. However, the initial degradation temperatures ($T_{-5\%}$) of the PFTNs are obviously higher than that of the pure PF (see Table III), indicating TiN nanoparticles inhibit the initial thermal degradation behavior of the PF. This phenomenon can be confirmed by the higher $T_{-10\%}$ and $T_{-30\%}$ for the PFTNs as compared with the pure PF. In addition, the PFTNs also show higher temperature of the maximum weight loss (T_{max1}) in first degradation stage in relation to the pure PF, further suggesting that TiN nanoparticles delay the initial thermal degradation stage. As show in Figure 8, the second degradation stages of the PFTNs are anticipated, which can be confirmed by the decreased T_{max2} after the addition of TiN nanoparticles. Even so, the PFTNs all present dramatically decreased weight loss rate (R_{max}) with respect to the pure PF. Moreover, the PFTNs leave more char residue (>55 wt %) than the pure PF (25.2 wt %) at 700 °C. The enhanced char residue of the PFTNs with respect to that of the pure (~30 wt %) are much higher than the addition of TiN nanoparticles (4 wt %). These results suggest that the addition of TiN nanoparticles can effectively protect the PF matrix from thermal degradation during heat process.

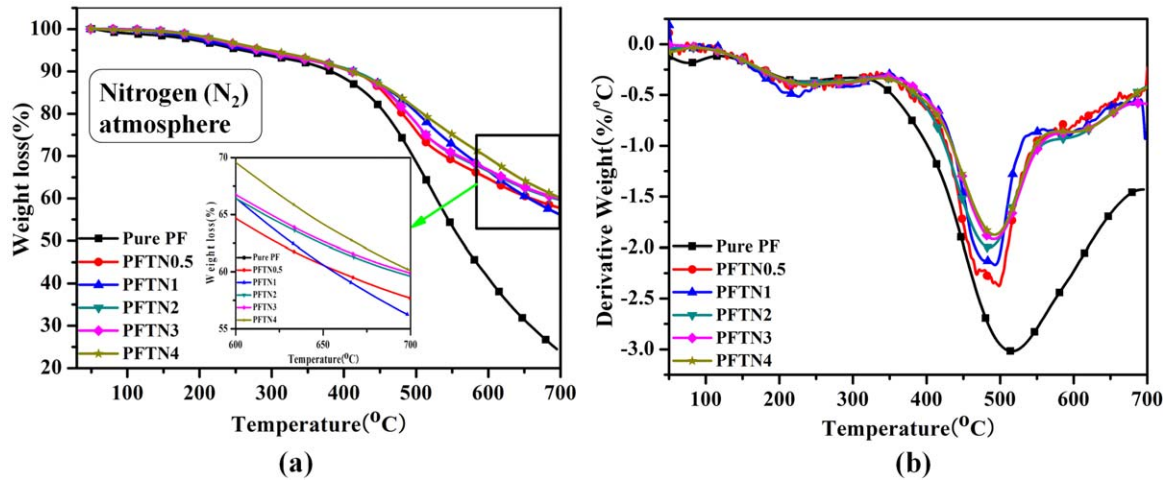

Figure 8. TGA (a) and DTG (b) curves of pure PF and PFTNs with different TiN content in nitrogen (N_2) atmosphere. [Color figure can be viewed in the online issue, which is available at wileyonlinelibrary.com.]

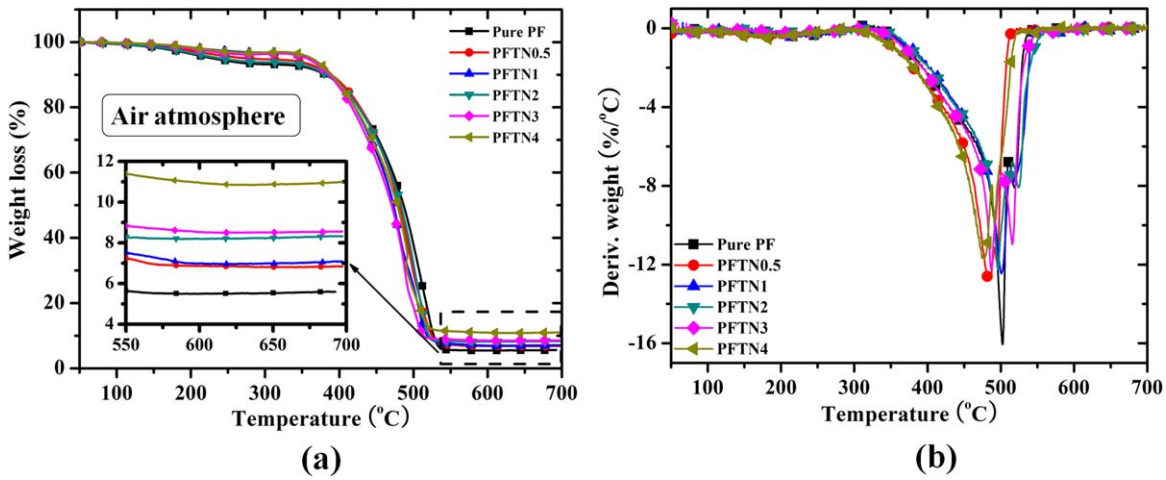

Figure 9. TGA (a) and DTG (b) curves of pure PF and PFTNs with different TiN content in air atmosphere. [Color figure can be viewed in the online issue, which is available at wileyonlinelibrary.com.]

The thermal stability of the pure PF and PFTN systems in air is also evaluated as shown in Figure 9 and some relevant TGA and DTG data of the pure PF and PFTNs are listed in Table IV. It can be seen that the decomposing process of the pure PF and PFTN systems is similar and the main decomposing stage is between 400 and 550 °C. Meanwhile, it is clearly seen that the main difference of the decomposing process is T_{max}, R_{max}, and char residue. However, compared with the pure PF, the introducing of nano-TiN significantly enhances the $T_{-5\%}$ of PF (Table IV), indicating nano-TiN inhibit the initial thermal decomposing behavior of PF.

From the DTG curves [Figure 9(b)], the T_{max} of PFTNs is all lower than that the pure PF and the PFTN4 shows the minimum T_{max}, indicating that the PFTN4 was firstly carbonized during the decomposing process, compared with other foams. This phenomenon can also be confirmed by the lower $T_{-10\%}$ and $T_{-30\%}$ for the PFTNs as compared with the pure PF. In addition, the weight loss rate and R_{max} of PFTN4 is lower than that of other foams between 400 and 550 °C, which is in accordance with the char residue data listed in Table IV. This result is mainly due to the embedded TiN nanoparticles in the cell walls of PFTNs, which can significantly keep inner phenolic material from burning by exterior heat energy during TGA heat process.

Moreover, the char residue of PFTNs increased with increasing of nano-TiN content as shown in Figure 9(a) and Table IV. The char residue at 700 °C for modified PF with 4 wt % nano-TiN is 98.2% higher than that of pure PF, which is much higher than the addition of nano-TiN (4 wt %). The results above indicate that the thermal stability of PFTNs is higher than that of pure PF. The PFTN4 shows the highest thermal stability in air atmosphere, which is in accordance with the TGA results in nitrogen atmosphere, indicating that the introducing of nano-TiN significantly enhances the thermal stability of PF.

Flame-Retardant Property

The flame retardant property of the pure PF and PFTN foams are evaluated by LOI and vertical flame test and the results are shown in Figure 10. It is clearly seen that all foam samples can pass V-0 rating, suggesting all PFTNs possess excellent flame-retardant property. As shown in Figure 10, the pure PF has a high LOI value of 28.3%. It is well known that phenolic foam holding a lot of benzene rings and a high proportion of carbon atoms easily carbonizes at high temperature.[54] By introducing TiN nanoparticles, the LOI values significantly increase. The possible reason is that, during the burning, TiN nanoparticles can separate the phenolic resin matrix from the air and heat. With the 2 wt % addition of nanoparticles, the LOI value reach to a maximum (34.2%), increased by 20.85% as compared with that of the neat PF foam. To further investigate the flame-retardant mechanism, the postburn char of all foams were

Table III. TGA and DTG Data in Nitrogen Atmosphere of Pure PF and PFTN Systems

Sample	$T_{-5\%}$ (°C)	$T_{-10\%}$ (°C)	$T_{-30\%}$ (°C)	T_{max1} (°C)	T_{max2} (°C)	R_{max} (%/°C)	Char residue (wt %) at 700 °C
PF	259.2	381.9	495.1	209.1	525.1	3.0	25.2
PFTN0.5	286.0	411.6	539.9	222.7	498.8	2.4	57.7
PFTN1	275.0	412.1	571.1	234.0	493.8	2.2	56.2
PFTN2	284.5	414.4	556.2	230.9	484.4	2.0	59.6
PFTN3	284.7	409.6	561.8	230.1	491.2	1.9	59.9
PFTN4	297.4	409.9	596.4	221.8	492.5	1.9	60.1

Table IV. TGA and DTG Data in Air Atmosphere of Pure PF and PFTN Systems

Sample	$T_{-5\%}$ (°C)	$T_{-10\%}$ (°C)	$T_{-30\%}$ (°C)	T_{max} (°C)	R_{max} (%/°C)	Char residue (wt %) at 700 °C
PF	267.1	381.5	452.9	502.4	16.0	5.6
PFTN0.5	286.2	389.3	450.9	485.4	12.7	6.9
PFTN1	311.5	390.6	444.2	500.2	12.4	7.2
PFTN2	328.4	393.9	450.8	496.2	12.2	8.3
PFTN3	343.4	395.4	440.9	487.5	12.2	8.6
PFTN4	352.6	401.9	445.0	477.1	11.7	11.1

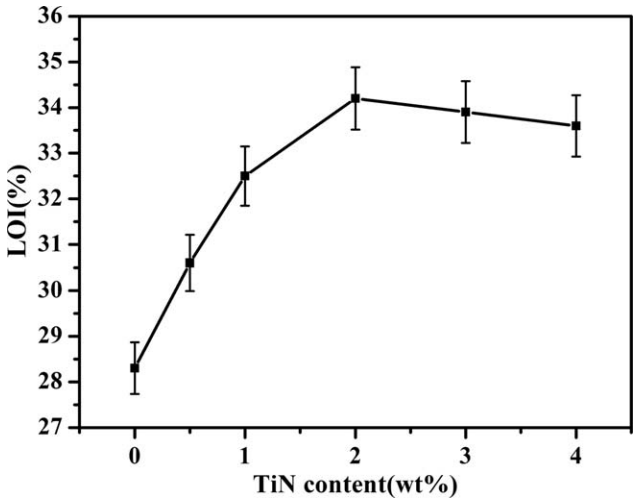

Figure 10. LOI of pure PF and modified PF with TiN nanoparticles. All samples have V-0 rating (UL-94 results).

observed by SEM, as shown in Figures 11 and 12. For the pure PF, the foam skeleton collapses after burning. However, the PFTNs preserve the intact foam skeleton after LOI test, which can also indicate that the PFTNs possess more efficient flame-retardant property. At high magnification, it can be easily found that the PFTNs preserve more intact char skeleton with respect to the pure PF. In particular, the PFTN2 leaves the char skeleton with most wide width (see Figure 12), corresponding with the highest LOI value. High nano-TiN content (3 or 4 wt %) in the system will partially agglomerate during the polymerization process of the phenolic/TiN composite resins, which will result in that the available nano-TiN content in the system less than its actual contents. In addition, we also calculated the densities of the residue chars after LOI. As shown in Table II, the char densities of the PFTNs are much higher than that of the pure PF, and the residue char density of the PFTN2 is the highest in relation to other foams, in good agreement with the above results.

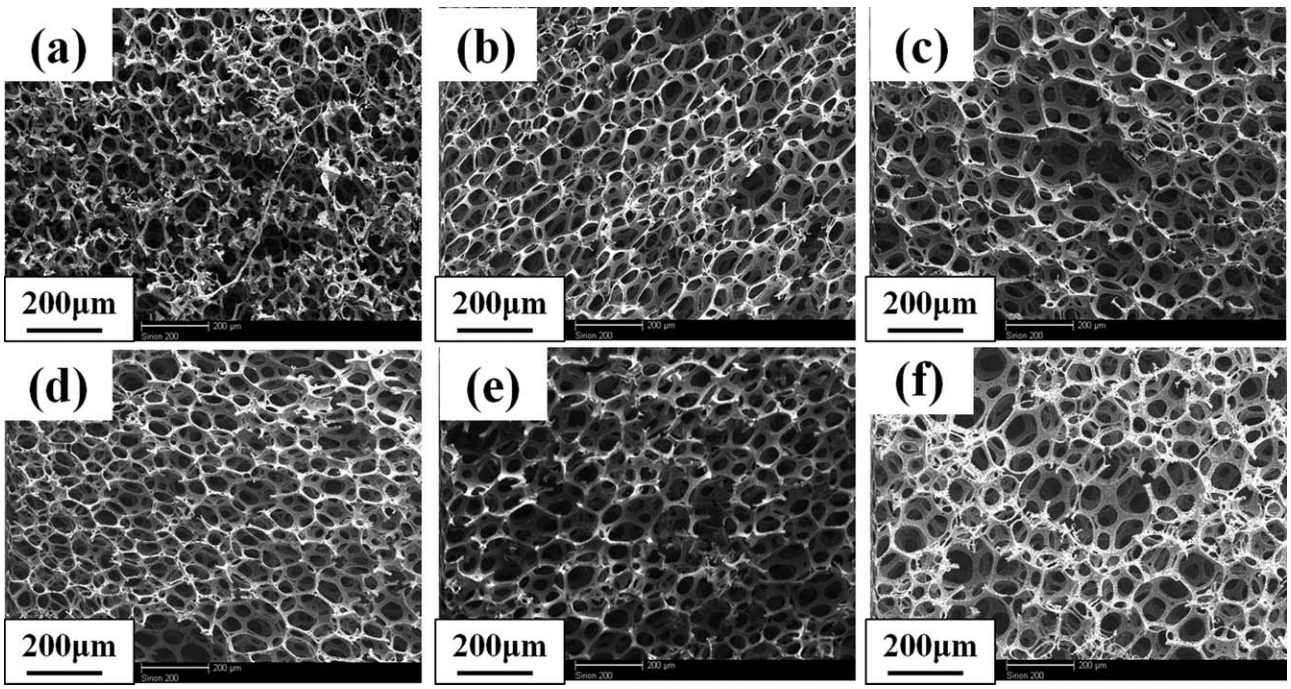

Figure 11. SEM images of (a) pure PF, (b) PFTN0.5, (c) PFTN1, (d) PFTN2, (e) PFTN3, and (f) PFTN4 after LOI tests (100×).

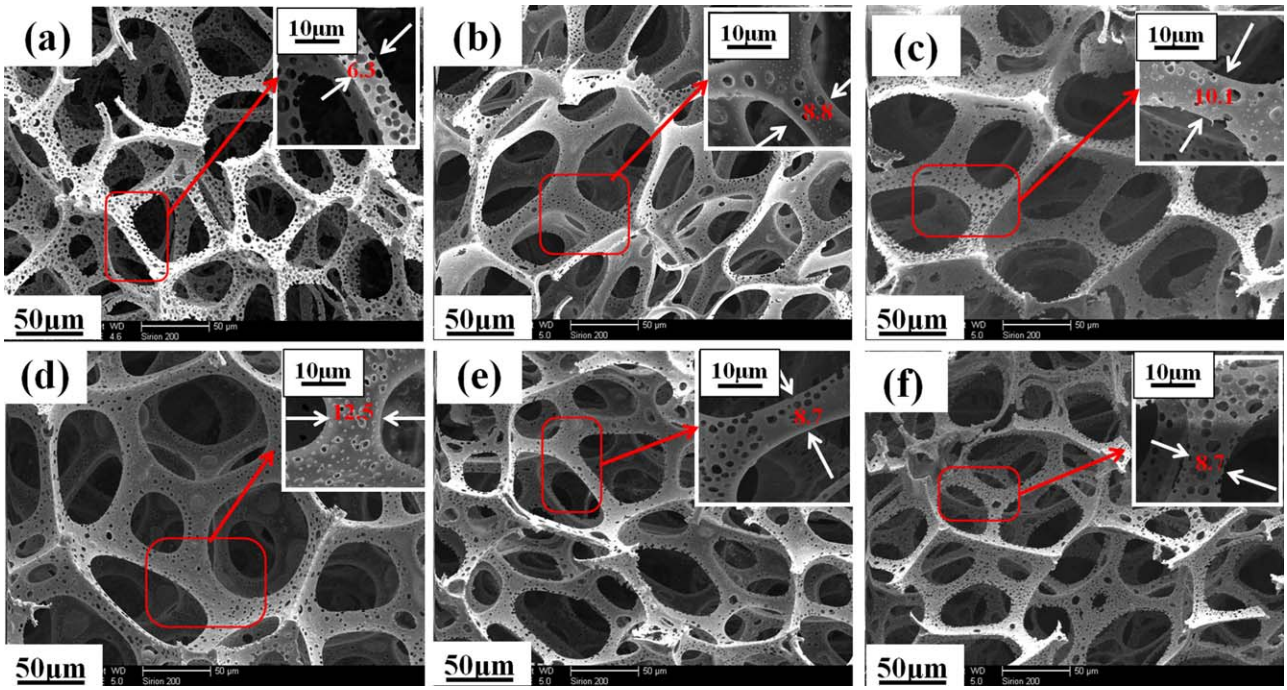

Figure 12. SEM images of (a) pure PF, (b) PFTN0.5, (c) PFTN1, (d) PFTN2, (e) PFTN3, and (f) PFTN4 after LOI tests (400×). [Color figure can be viewed in the online issue, which is available at wileyonlinelibrary.com.]

CONCLUSIONS

In this work, phenolic foam modified by TiN nanoparticles (PFTNs) were fabricated by blending the phenolic resin/TiN nanocomposites (synthesized by *in situ* polymerization) (PRTNs) with additives through chemical foaming to improve their thermal insulating, flame-retardant, and mechanical performances. The effects of the TiN nanoparticles on the porosity, cell density and morphology of PFTNs, and its connection with physical properties were investigated. Based on the experiments, the following results were acquired.

SEM results indicated that the PFTNs showed more uniform cell morphology. Moreover, the PFTNs have narrower cell sizes distributions and smaller mean cell sizes, compared with pure PF.

The results of UL-94 vertical flame tests showed that all foam samples can pass V-0 rating, revealing that all foams have excellent flame-retardant performances. Furthermore, by introducing the TiN nanoparticles, the LOI values of the PFTNs are higher than that of the pure PF. Of special note was that the PFTN2, which has high char skeleton density, intact and wider char skeleton, had the highest LOI value that increased by 20.9% as compared with that of the pure PF. Thermal stabilities in nitrogen and air atmosphere of the PFTNs are all much higher than that of the pure PF, indicating that nano-TiN can significantly improve the thermal stability of the PF. In addition, slight nano-TiN content can improve the mechanical properties of the PF to a certain extent, but high content of nano-TiN (4 wt %) will decrease the mechanical properties.

The most important results were that the PFTNs exhibit more excellent thermal insulating performance by the introduction of TiN nanoparticles. The thermal conductivity of the pure PF increases as the temperature increases during the temperature range of −20 to 60 °C. Moreover, the thermal conductivity of the PFTNs increased gradually with the increase of the temperature at the range of −20 to 20 °C. However, further raise in the temperature (30–60 °C) decreases the thermal conductivity of the PFTNs. In addition, the thermal conductivities of the PFTNs are all lower than that of the pure PF at different temperatures. The PFTN1 has the lowest thermal conductivity which showed decrease of 23.7% at −20 °C and 19.4% at 20 °C, respectively, in relation to the pure PF, because PFTN1 possesses a more uniform cells distribution, smaller mean cell size, narrower cell sizes distribution, higher porosity, and cell density. At 60 °C, the PFTN4 has a lowest thermal conductivity due to the high additive content of TiN nanoparticles which has radiant barrier function.

From this study, it was concluded that the introduction of TiN nanoparticles can decrease the thermal conductivity and improve the flame-retardant properties. Especially, the thermal conductivity of PFTNs decreases as the temperature increases at 30–60 °C.

ACKNOWLEDGMENTS

The authors gratefully acknowledge the financial support from the National Natural Science Foundation of China (No.21204090 and No.51303182).

REFERENCES

1. Vaikhanski, L.; Nutt, S. R. *Compos. Part A* **2003**, *34*, 755.
2. Zeng, C.; Hossieny, N.; Zhang, C.; Wang, B. *Polymer* **2010**, *51*, 655.

3. Huang, H. X.; Xu, H. F. *Polym. Adv. Technol.* **2011**, *22*, 822.
4. Yen, Y. C.; Lee, T.; Chiu, D.; Chang, F. C.; Lee, L. *J. Cell. Plast.* **2014**, *50*, 437.
5. Wong, C. M.; Hung, M. L. *J. Cell. Plast.* **2008**, *44*, 239.
6. Luo, F.; Wu, K.; Lu, M.; Nie, S.; Li, X.; Guan, X. *J. Therm. Anal. Calorim.* **2015**, *120*, 1327.
7. Kuncir, E. J.; Wirta, R. W.; Golbranson, F. L. *J. Rehabil. Res. Dev.* **1990**, *27*, 229.
8. Luong, D. D.; Pinisetty, D.; Gupta, N. *Compos. Part B* **2013**, *44*, 403.
9. Rodriguez-Perez, M. A.; Gonzalez-Pena, J. I.; Witten, N.; de Saja, J. A. *Cell. Polym.* **2002**, *21*, 165.
10. Yang, H.; Wang, X.; Yuan, H.; Song, L.; Hu, Y.; Yuen, R. K. K. *J. Polym. Res.* **2012**, *19*, 1.
11. Thirumal, M.; Singha, N. K.; Khastgir, D.; Manjunath, B. S.; Naik, Y. P. *J. Appl. Polym. Sci.* **2010**, *116*, 2260.
12. Thirumal, M.; Khastgir, D.; Singha, N. K.; Manjunath, B. S.; Naik, Y. P. *J. Appl. Polym. Sci.* **2008**, *110*, 2586.
13. Zhou, J.; Yao, Z.; Chen, Y.; Wei, D.; Wu, Y. *Mater. Des.* **2013**, *51*, 131.
14. Liu, L.; Fu, M.; Wang, Z. *Ind. Eng. Chem. Res.* **2015**, *54*, 1962.
15. Sui, X.; Wang, Z. *Polym. Adv. Technol.* **2013**, *24*, 593.
16. Auad, M. L.; Zhao, L.; Shen, H.; Nutt, S. R.; Sorathia, U. *J. Appl. Polym. Sci.* **2007**, *104*, 1399.
17. Shen, H.; Lavoie, A. J.; Nutt, S. R. *Compos. Part A* **2003**, *34*, 941.
18. Del Saz-Orozco, B.; Alonso, M. V.; Oliet, M.; Domínguez, J. C.; Rodriguez, F. *Compos. Part B* **2014**, *56*, 546.
19. Ma, Y.; Wang, J.; Xu, Y.; Wang, C.; Chu, F. *J. Therm. Anal. Calorim.* **2013**, *114*, 1143.
20. Lei, S.; Guo, Q.; Shi, J.; Liu, L. *Carbon* **2010**, *48*, 1686.
21. Yang, Z. J.; Yuan, L. L.; Gu, Y. Z.; Li, M.; Sun, Z. J.; Zhang, Z. G. *J. Appl. Polym. Sci.* **2013**, *130*, 1479.
22. Zhou, J.; Yao, Z.; Chen, Y.; Wei, D.; Xu, T. *Polym. Compos.* **2014**, *35*, 581.
23. Kim, B. G.; Lee, D. G. *J. Mater. Process. Technol.* **2008**, *201*, 8334.
24. Song, S. A.; Chung, Y. S.; Kim, S. S. *Compos. Sci. Technol.* **2014**, *103*, 85.
25. Li, W. L.; Lin, Q.; Yan, M. F.; Zou, Y. S. *J. Appl. Polym. Sci.* **2003**, *90*, 2333.
26. Li, Q.; Chen, L.; Zhang, J.; Zheng, K.; Zhang, X.; Fang, F.; Tian, X. *Polym. Eng. Sci.* **2015**, *55*, 2783.
27. Li, Q.; Chen, L.; Li, X.; Zhang, J.; Zhang, X.; Zheng, K.; Fang, F.; Zhou, H.; Tian, X. *Compos. Part A* **2016**, *82*, 214.
28. Lei, S.; Guo, Q.; Zhang, D.; Shi, J.; Liu, L.; Wei, X. *J. Appl. Polym. Sci.* **2010**, *117*, 3545.
29. Song, S. A.; Oh, H. J.; Kim, B. G.; Kim, S. S. *Compos. Sci. Technol.* **2013**, *76*, 45.
30. Zach, J.; Hroudová, J.; Brožovský, J.; Krejza, Z.; Gailius, A. *Proc. Eng.* **2013**, *57*, 1288.
31. Reichenauer, G.; Heinemann, U.; Ebert, H. P. *Colloids Surf. A* **2007**, *300*, 204.
32. Jacksont, G. V.; Butler, J. R. J. *J. Phys. D: Appl. Phys.* **1993**, *26*, 740.
33. Braginsky, L.; Shklover, V.; Witz, G.; Bossmann, H. P. *Phys. Rev. B* **2007**, *75*, 094301.
34. Tseng, C. J.; Kuo, K. T. *J. Chin. Inst. Eng.* **2002**, *25*, 753.
35. de Carvalho, G.; Pimenta, J. A.; dos Santos, W. N.; Frollini, E. *Polym. Plast. Technol. Eng.* **2003**, *42*, 605.
36. Wang, B.; Li, H.; Zhang, Y.; Li, Y.; Liu, C. *Mater. Chin.* **2013**, *32*, 641.
37. Abedi, S.; Abdouss, M.; Daftari-Besheli, M.; Moghimi, A.; Ghafelehbashi, S. M.; Pourian, M. A. *J. Inorg. Organmet. Polym.* **2014**, *24*, 416.
38. Nair, C. P. R.; Bindu, R. L.; Ninan, K. N. *Polym. Degrad. Stabil.* **2001**, *73*, 251.
39. Lin, R.; Fang, L.; Li, X.; Xi, Y.; Zhang, S.; Sun, P. *Polym. J.* **2006**, *38*, 178.
40. Wei, D.; Li, D.; Zhang, L.; Zhao, Z.; Ao, Y. *Proc. Eng.* **2012**, *27*, 374.
41. Selvapandiyan, M.; Arumugam, J.; Sundaramoorthi, P.; Sudhakar, S. *J. Alloys Compd.* **2013**, *558*, 34.
42. Vasu, K.; Krishna, M. G.; Padmanabhan, K. A. *Thin Solid Films* **2011**, *519*, 7702.
43. Ohnishi, R.; Katayama, M.; Cha, D.; Takanabe, K.; Kubota, J.; Domen, K. *J. Electrochem. Soc.* **2013**, *160*, F501.
44. Chen, K. P.; Tian, C. R.; Lu, A.; Zhou, Q. M.; Jia, X. R.; Wang, J. H. *J. Appl. Polym. Sci.* **2014**, *131*, 3424.
45. Kim, J.; Lee, J. H.; Song, T. H. *Int. J. Heat Mass Transf.* **2012**, *55*, 5343.
46. Tseng, C.; Yamaguchi, M.; Ohmori, T. *Cryogenics* **1997**, *37*, 305.
47. Thirumal, M.; Khastgir, D.; Singha, N. K.; Manjunath, B.; Naik, Y. *J. Appl. Polym. Sci.* **2008**, *108*, 1810.
48. Anderson, D. R. *Chem. Rev.* **1966**, *66*, 677.
49. Tseng, C. J.; Kuo, K. T. *J. Quant. Spectrosc. Radiat. Transf.* **2002**, *72*, 349.
50. Li, Q.; Chen, L.; Ding, J.; Zhang, J.; Li, X.; Zheng, K.; Zhang, X.; Tian, X. *Carbon* **2016**, *104*, 90.
51. Samani, M. K.; Ding, X. Z.; Khosravian, N.; Amin-Ahmadi, B.; Yi, Y.; Chen, G.; Neyts, E. C.; Bogaerts, A.; Tay, B. K. *Thin Solid Films* **2015**, *578*, 133.
52. Yang, C.; Zhuang, Z. H.; Yang, Z. G. *J. Appl. Polym. Sci.* **2014**, *131*, DOI: 10.1002/app.39734.
53. Rangari, V. K.; Hassan, T. A.; Zhou, Y.; Mahfuz, H.; Jeelani, S.; Prorok, B. C. *J. Appl. Polym. Sci.* **2007**, *103*, 308.
54. Yuan, H.; Xing, W.; Yang, H.; Song, L.; Hu, Y.; Yeoh, G. H. *Polym. Int.* **2013**, *62*, 273.